ROBUST AND EFFICIENT MULTISTAGE BRAKING SYSTEM FOR CABLE DRIVEN ROBOTS

*Michael Fanton[1], *Paul Glick, [2]

Jonathan Bruce,[3] Ken Caluwaerts,[3] Jeffery Friesen,[3] Vytas Sunspiral,[3]

[1]*Stanford University, USA, E-mail: mfanton@stanford.edu*

[2]*University of California, San Diego, USA , E-mail: pglick@ucsd.edu*

[3]*NASA Ames Research Center, USA *Equal Contribution, Authors listed alphabetically*

ABSTRACT

We present a Multistage Braking System (MBS), optimized for the needs of NASA's SUPERball tensegrity robot, which addresses a range of issues common to cable driven robotic drivetrains. The system works to reduce power consumption, provide constant motor protection, and dissipate large but infrequent impact forces. The Spherical Underactuated Planetary Exploration Robot ball (SUPERball) from NASA Ames Research Center's Dynamic Tensegrity Robotics Lab is designed to land at terminal velocity on other planets as tensegrity structures can withstand significant impact shocks. Furthermore, SUPERball may experience subsequent impact events as its mission may include exploring treacherous terrain such as ledges and canyons. However, the drivetrain still must be protected from residual forces reflected into the gearboxes and motors. Thus, SUPERball must balance the ability to withstand occasional but extreme landing forces with efficient and robust locomotion. Using the presented MBS, comprised of a Bi-Directional Self-Locking Clutch (BDSLC) for routine locomotion and a Retractable Jaw Clutch (RJC) for large impact events, SUPERball will be able to traverse previously inaccessible extraterrestrial locations with a lower average power consumption.

1 INTRODUCTION

In this paper we propose a Multistage Braking System (MBS), composed of two rotary locking devices to be used in series, designed and optimized for SUPERball. SUPERball is a cable-driven planetary lander and exploration robot developed at NASA Ames Dynamic Tensegrity Robotics Laboratory. Designed using the structural concept of tensegrity [2], SUPERball is a compliant, robust, and weight-efficient robot, with dynamic locomotion and the potential to deploy without external landing equipment [3, 4]. Using motors to vary cable tension, the robot can be actuated to various stable configurations; by altering its center of gravity, SUPERball can roll in a specified direction.

Tensegrity robots are naturally well suited for space applications. Due to their small launch package, high mass efficiency, and reliability, tensegrity systems have been envisioned to explore caves, form deployable antennas, function as spines to be used in legged robots or exoskeletons, enable dynamic wings, and act as compliant joints in humanoid robots [1, 2 ,3]. Our mechanism design has been optimized for NASA's SUPERball robot, a tensegrity planetary lander and exploration rover designed to be sent to explore the surface of Saturn's largest moon, Titan.

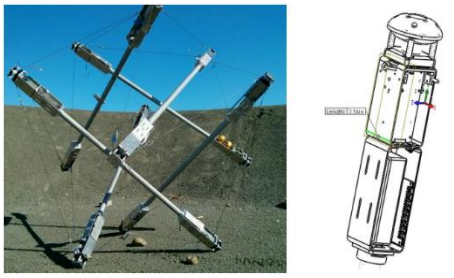

(a) NASA's SUPERball (b) SUPERball endcap

Figure 1: NASA's SUPERball Tensegrity Robot

Braking and locking mechanisms provide a wide variety of valuable functions in robotic systems, for instance locking an appendage in a specific configuration or delaying the energy release of a spring. Though braking systems have been extensively studied for conventional rigid robots, there has been a recent surge of interest in locking mechanisms for cable-actuated robots. Efficient and reliable braking systems can provide numerous benefits for cable-driven robots: protecting actuators from large cable forces, reducing power consumption by improving tension control, and improving safety and reliability through fail-safe brakes [1].

As "tensegrity" robots are transitioning from academic concepts to real world applications, there has been an increase in demand for new engineering innovations and novel mechanisms to allow these machines to perform to their fullest potential [5]. Two primary challenges pertinent to tensegrity robots have created a pressing need for the MBS presented in this paper. The first challenge is a need to reduce power consumption. Tensegrity robots are flexible and must be able to both change position and hold pose. Contracting a tensile cable always consumes power; however, simply holding a pose

also currently requires active motor input to prevent backdriving of the cables. The second challenge is the need to adequately protect the drivetrain from large impact forces. Tensegrity structures have an exceptional strength to weight ratio allowing the potential to withstand significant impacts [3, 4]. However, as tensegrities get heavier, they require increased stiffness in their compliant members to maintain structure stability. Stiffer systems naturally create larger cable tensions under impact. The MBS presented provides SUPERball with excellent drivetrain impact protection, allows the motors to shut down when holding pose, and does so with only minimal increases to size, weight, and inertia.

The primary braking system of the MBS is a bi-directional self-locking clutch (BDSLC), which utilizes a known cam-wedge concept to efficiently transmit input motion to the output shaft while blocking output loads from affecting the input, allowing the motors to be turned off when SUPERball is not moving. The BDSLC is designed to handle output loads up to 25 Nm, only weighs 225 g, and requires no input power. An initial prototype of the BDSLC has been built which validates the concept for the scale of the MBS, but needs further engineering refinement to meet the final desired specifications. This mechanism will allow SUPERball to shut down its twelve 100 watt motors while holding a pose.

The secondary braking system is a bi-stable, retractable jaw clutch (RJC). This heavy duty braking mechanism is actuated by a lightweight motor, and only requires power to engage or disengage. Designed to have minimal impact on normal locomotion, with a total weight of 61.1 g and rotational inertia of 31.4 gcm^2, the RJC can withstand torques of over 400 Nm, and can engage in under 150 ms. This device will protect SUPERball's key drivetrain components from large impact forces during deployment and unexpected falls.

The braking systems presented in this paper are the first cable-locking mechanisms optimized for tensegrity-based robots, and to our knowledge, the integrated MBS drivetrain would be the first system that combines passive non-back-drivability with robust protection for cable-driven robots. The design of both devices can be easily adjusted and scaled for other applications requiring rotary locking.

2 PREVIOUS WORK

During routine locomotion, the SUPERball drivetrain can be expected to experience torques of up to 25 Nm due to cable back driving [Appendix]. Assuming a worst-case fall scenario at terminal velocity, the SUPERball drivetrain could be exposed to much larger cable torques of up to 400 Nm [Appendix]. These two significantly different design requirements motivate two separate braking devices: a smaller, passive device to prevent backdrivability of the cables, and a heavy-duty brake for fall protection.

Non-backdrivable mechanisms have been long used in a multitude of rotary-driven applications requiring output position holding for energy management, fail safe braking, and motor protection [1]. One common approach to achieve non-backdrivability is the use of a very high gear reduction ratio, though this concept is not suited for cable driven robotics as it suffers from high backlash and controllability issues [1, 6]. Other common self-locking devices are lead-screws and worm drives. Though simple in design and implementation, these gears are also unsuitable for most robots due to their low efficiency, low speed capabilities, increased heat generation, and relatively high gear ratios [6, 7]. A more recent approach to prevent back-drivability is with specialized roller clutches [6, 9, 10]. These clutches prevent back-driven torques with rolling elements, held in place by a compliant material, which wedge between an outer race and inner cam surface. These non-backdrivable clutches are commonly used in industrial applications in the past, but more recently have been applied to robotic systems [6, 9, 11 12].

A variety of more heavy duty mechanical rotary braking devices exist for robotic systems, and can be categorized into three main categories: friction-based, mechanical, and singularity locking [1]. Friction-based locking devices include disk brakes, electromagnetic brakes, and drum brakes, and are limited by the amount of applied normal force; for SUPERball's application, these normal forces would need to be too large be rated to over 400 Nm. Singularity locking devices, such as the four bar linkage used in [14], exhibit high locking torque, but only lock in their singular position [1], and thus are also unsuitable for SUPERball. Mechanical locking devices utilize a physical obstruction to create a braking force. Common examples used in robotic applications include latches and ratchets [15, 16, 17, 18], and jaw (dog) clutches [19]. A jaw clutch consists of axially protruding teeth that mesh together to lock relative rotational motion between each other. These devices have a much higher locking torque-to-weight ratio compared to latches and ratchets, since the load in distributed over multiple thick teeth. Because of this, at a given torque load it is possible to significantly decrease the radius and inertia of the device compared to other mechanical braking devices [1].

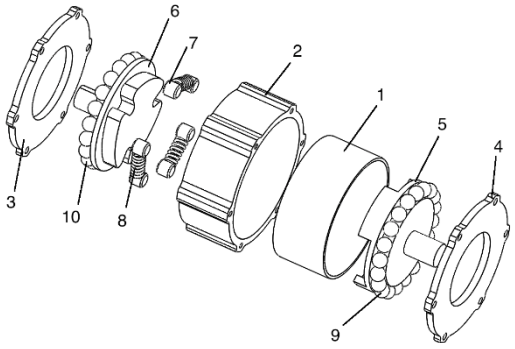

Figure 2: Exploded view of the BDSLC

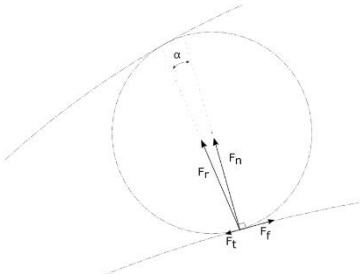

Figure 4: FBD of wedged roller

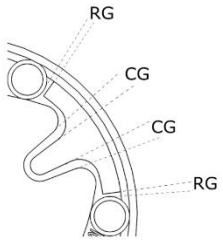

Figure 5: BDSLC gap notation

3 BDLSC MECHANISM AND ANALYSIS

3.1 BDSLC Mechanism Overview

An exploded view of the entire BDSLC mechanism is shown in Figure 2. The chassis of the BDSLC is comprised of a precision-machined aluminum outer race (1), a 3D-printed ABS outer enclosure (2), and two Delrin end plates (3) (4). The outer chassis encompasses the inner components: the aluminum input and output shafts (5) and (6) respectively, steel wedge rollers (7), compression springs (8), and alignment ball bearings (9) (10).

A cross sectional view of the BDSLC is shown in Figure 3a. In this view we see the input teeth (11), which are connected directly to the input shaft. Likewise, the output cam (12), is connected directly to the output shaft. The rollers (7), held in place by compression springs (8), wedge between the output cam and the outer race. The wedged rollers prevent the output shaft from moving both clockwise and counter-clockwise, therefore preventing output loads from transmitting torque to the input. However when the input shaft rotates in either direction, the input teeth displace the rollers from their wedged position, allowing the teeth to engage with the cam thus permitting torque to be transmitted to the output shaft. Figure 3b shows the cross section view of the system when engaged with an input torque in the counter-clockwise direction.

There are various geometric design parameters which are vital to proper operation of the BDSLC.

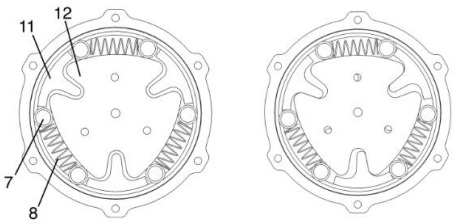

Figure 3: Cross-section view of BDSLC

The three principal design parameters are summarized below, refer to each subsection for further details.

3.2 BDLSC Self-Wedging Analysis

There are two main criteria that must be met in order to ensure non-backdrivability of the output [9]. Section 3.2 overviews and analyzes the first: that the geometry of the cam, outer race, and rollers must produce a self-wedging system. For this to occur, the frictional forces acting on the roller must equal the tangential forces acting from the cam and outer race onto the roller.

The force body diagram in Figure 4 shows the forces acting between a wedged roller and the output cam. While fully wedged, the forces between the roller and the outer race must be equal and opposite to the forces between the roller and cam; thus, for simplicity, only the forces between the roller and the cam are shown. F_n is the normal force acting from the point of contact to the center of the roller. F_t is the tangential force acting from the cam onto the roller perpendicular to F_n. F_r is the resultant of the F_n and F_t force vectors, which acts along the line connecting the two points of contact on the roller. The angle α is the angle between the vector of F_n and the vector of F_r. This angle is essentially a measure the parallelism between the cam and outer race surfaces, and is vital for determining wedging [9].

It is clear from the FBD that the frictional force, F_f, must be able to counteract the tangent force, F_t, or the roller will slip clockwise and become unwedged. With a known output torque and angle α, F_r can be found and resolved into its components F_t and F_n. As derived in [9], in order for self-wedging to occur, we get:

$$F_f > F_t;\ \ \mu_s F_r \cos(\alpha) > F_r \sin(\alpha);\ \ \mu_s > \tan(\alpha)$$

3.3 BDLSC Hertizan Stress Analysis

The second design requirement to prevent back-drivability of the output is that there must be a sufficient roller gap to handle material deformation. When force is applied, contact

stresses between the roller, cam, and outer race surfaces create small surface deflections, closing the gap between the roller and the surface of the teeth (denoted as the roller gap, or RG in Figure 5). If these surface deformations are too large the gap between the roller and the teeth can completely close, allowing the output to transmit torques to the input thereby allowing back-drivability. The reduction in RG gap size given a decrease in roller radius Δr can be approximated using the following equation:

$$\Delta RG = \Delta r\left(\frac{1}{\sin\alpha} - 1\right)$$

Heinrich Hertz established the classical theory for determining compressive surface stresses and deformations between non-adhesive, elastic bodies [13]. Hertz stated that the contact line between two cylinders is compressed into a small elliptical region with a half-width of b:

$$b = \sqrt{\frac{4 * F * R_c}{\pi * E_c}}$$

Where

$$\frac{1}{R_c} = \frac{1}{R_1} + \frac{1}{R_2}$$

$$\frac{1}{E_c} = \frac{1 - v_1^2}{E_1} + \frac{1 - v_2^2}{E_2}$$

And L is the length of the contact line.

By integrating the strain from the point of contact to distant points on the body, the displacement, or the approach of the centers of the two bodies, can be given by [13]:

$$\delta \approx \frac{2F}{\pi L}\left(\left(\frac{1 - v_1^2}{E_1} * \ln\frac{4R_1}{b} - \frac{1}{2}\right) + \left(\frac{1 - v_2^2}{E_2} * \ln\frac{4R_2}{b} - \frac{1}{2}\right)\right)$$

The change in roller diameter can thus be approximated as:

$$\delta_{total} = \delta_{camroller} + \delta_{Oroller}$$

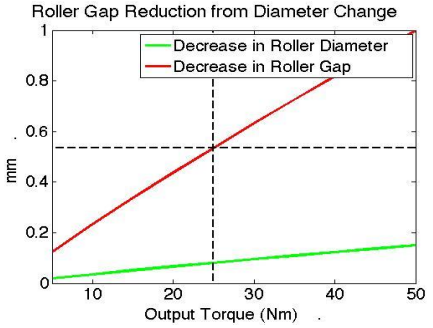

Figure 6: Change in roller diameter vs RG at α = 4

Figure 6 graphs the change in the roller diameters versus the change in the RG for various output torques given α=4°, (the choice of α=4° is overviewed in subsection 3.5). According to Hertz's theory, a torque of 25 Nm would produce an approximate deflection of .09 mm in the roller, reducing RG by .55 mm. Therefore, the RG must be at least .55 mm to be rated to 25 Nm.

3.4 BDLSC Backlash Analysis

The final consideration in the design process of the BDSLC geometry was backlash of the system. Due to BDSLC geometry, input and output backlash are not the same. Input backlash is a function of the RG and input tooth contact radius. The BDSLC theoretically has zero output backlash. The compression springs hold the rollers in a wedged position, so when a load is applied to the output it is instantly locked. This quality is particularly desirable for tensegrity robots, because it is important that the strings hold a specific amount of tension or maintain a precise length to realize a certain configuration accurately.

There is unavoidable input backlash on the BDSLC due to the roller gap and cam gap. A minimum RG of 0.55 mm is needed to overcome deflections in the roller from 25 Nm of torque. The cam gap, or CG (as shown in Figure 5), is required to allow the teeth to push the rollers out of place before engaging with the output. The CG must be larger than the RG, or else the input will engage the output before the output is unlocked. Conversely, a CG that is too small can cause the rollers to only partially un-wedge, creating large friction when the input drives the output.

The input backlash is simply the CG in degrees, or the amount of rotation the input will need before engaging with the output. Knowing the linear distance between the tooth and the output shaft and the minimum radius at which the teeth engage the cam, the backlash can be calculated with the following equation:

$$B = \frac{CG * 180}{R_a * \pi}$$

Several design improvements were implemented to minimize the amount of input backlash. The input teeth were moved as far from the center of rotation as possible; creating a smaller backlash at a given gap size. The teeth and output shaft surfaces are angled radially so the entire tooth surface engages the cam instead of just the most central point.

3.5 BDLSC Design Summary

The coefficient of friction between the 6061

aluminum outer race and the steel rollers was empirically estimated to be about 0.17 dictating a maximum α of 9.6°. To account for a decrease in friction due to wear over time, we chose an α of 4°. An RG of .55 mm was used to ensure a 25 Nm torque rating. A CG of 1.05 mm was found to be large enough to fully un-wedge the rollers with an acceptably low input backlash ~4°.

4 BDSLC EVALUATION AND RESULTS

The BDSLC was iteratively developed in ABS plastic and in 6061-aluminum to a 5 mil tolerance. Initial results of the prototype are presented below. The tests validate the two main requirements of BDSLC: functioning self-wedging and a proper RG. The device successfully stopped the maximum, 12 Nm, of torque we were able to apply under the current test procedure. As there was no slipping or unlocking whatsoever, this value will increase with an improved test setup. Efficiency is currently at an unacceptably low value of 44% but this is due to machining tolerances of the chassis, and is not inherent to BDSLC geometry.

4.1 Maximum Torque

An initial torque risk reduction test was performed on the BDSLC to ensure that the device could withstand our predicted output loads without damage to the inner components. The BDSLC was mounted onto an acrylic base with ABS housing, and the output shaft was loaded via a clamped lever arm connected to weights. Under these conditions, the system successfully handled over 12 Nm of torque before the 3D printed chassis itself broke. Even with this load no slipping or unlocking was observed. A stronger chassis will allow the system to continue wedging far past 12 Nm. These initial results validate the torque rating design analysis within a factor of two and will be further tested as development continues.

4.2 Efficiency

The BDSLC will be most inefficient at no load. [6] To quantify this loss of energy, we created a test set-up consisting of a Maxon motor (20 Watts, part number 118752) with a 14:1 gearbox (part number 144029) monitored with an AS5048B magnetic encoder. The rotational velocity was sampled at various input voltages while monitoring current. The BDSLC was then attached to the motor and the rotational velocity was again measured at the same voltages. The efficiency can then be estimated with the following ratio:

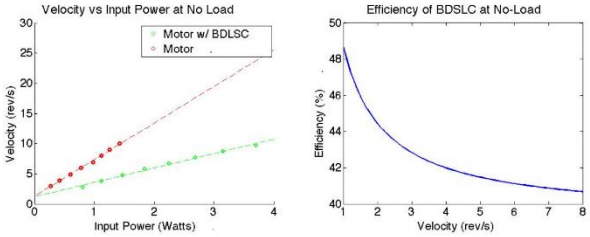

(a) Relative velocities (b) Corresponding efficiency

Figure 7: Efficiency of BDSLC at no-load

$$E = \frac{W_{noload}}{W_{BDSLC}}$$

Figure 7b graphs the efficiency at various input voltages, with an average no-load efficiency of 44%. As seen in [6], initial prototypes of such rotational devices often waste 30% of the system energy. This can be due to misalignment, improper tolerances, and losses due to high surface roughness. Additionally, the thin outer race of our prototype bent when under load and further impacted performance; this could be easily remedied by using a thicker outer shell. Finally, if these engineering issues were resolved, peak efficiency could be boosted by using brass rollers and ball bearings. Brass rollers would slightly decrease the maximum torque rating, but this could by counteracted by using an 8 roller design, which was not possible given our limited machining access.

5 RJC MECHANISM AND ANALYSIS

5.1 RJC Mechanism Overview

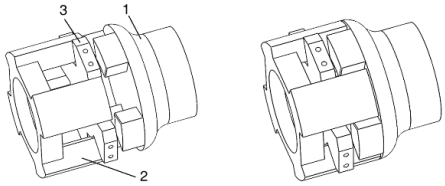

(a) Jaw clutch disengaged (b) Jaw clutch engaged

Figure 8: RJC components

The RJC is comprised of three main components, simplified and shown in Figure 9. The claw (1) is the rotating component that needs to be locked; in SUPERball application, the claw would be directly integrated onto the end of the cable spool. The jaw (2) is the component that engages linearly with the claw to lock it in place. The spider (3) is a static component, externally fixed, that acts as a linear bearing for the jaw while radially constraining it. An extension spring connects the jaw and the spider to increase engagement time and to create a bi-stable system, as described below. Figure 8a shows the system in a disengaged state, and Figure 8b shows it with the jaw engaged.

The jaw is linearly engaged and disengaged with a small, geared motor. A novel, modified "Scotch yoke" mechanism is used to convert the rotational motion of the geared motor to linear motion of the jaw. An outline of a traditional "Sctoch yoke" mechanism is shown in Figure 9a; a rotating pin is coupled with a linear sliding shaft through a slot, and the shaft can be reciprocated through rotational motion of the pin (or vise versa).

The modified "Scotch yoke" mechanism is depicted in Figure 9b. The slot has been shortened on one side to create backstops, which correspond to the engaged and disengaged dwell positions. At the top dwell, the spring force drives the motor pin into the backstop, thus passively locking the shaft in place until the motor drives it clockwise. At the bottom dwell, the spring provides a force downwards to lock the jaw in position. The geared motor is equipped with an encoder to sense unwanted changes in angles due to large vibrations, and can be turned on to provide additional locking torque if necessary.

5.2 RJC Strength Analysis

The geometry of each jaw tooth is defined by an inner radius *ID*, outer radius *OD*, height *h*, and cross sectional area A_c. 6061-aluminum was selected for the analysis because it is a strong yet lightweight material satisfactory for this application. The yield stress, S_c of 6061-T6 aluminum is 207 MPa [20]. At a given torque rating, one can calculate the required minimum horizontal cross sectional area and tooth height. If the final design exceeds the minimum calculated value for these two variables, the part will not fail due to shearing or crushing [21].

The yield torque τ can be from using equation 14 and the minimum height using equations 15 and 16. *n* is the number of teeth [21].

$$(OD^2 - ID^2) * (OD + ID) = \frac{32\tau}{\pi * S_c}$$

$$A_c = \frac{4\tau}{n * (OD + ID) * S_c}$$

$$h = \frac{A_c}{OD - ID}$$

The desired maximum torque rating is 400 Nm. Since the jaw component will be wedged between two offset pieces, its teeth will experience additional shear force. Therefore, at minimal expense, the component dimensions were selected to meet an 800 Nm torque rating; these components ultimately only added a combined mass of 61.11 g and inertia of 31.43 gcm^2. To fulfill the design requirements outlined in the above equations, an outer and inner diameter of 33 and 17 mm respectively and tooth height of

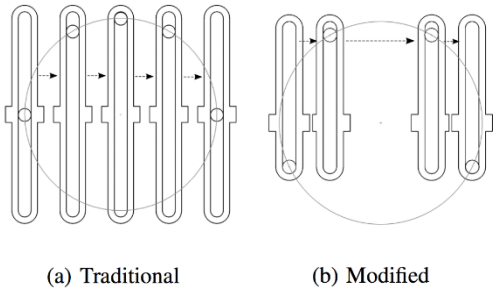

Figure 9: a) Traditional scotch yoke mechanism. b) Modified scotch yoke used on RJC

5mm were selected for their small package size. This results in yield strength of 812 Nm.

5.3 RJC Engagement Time

It is vital that the RJC can engage quickly during unexpected falls above 5 meters, at which the BDSLC is overwhelmed [Appendix]. The approximate RJC engagement time can be found using kinematics. The motor provides 0.11 Nm of torque at a radius of 7.2 mm, and the mass of the jaw is 20.4 g. Frictional forces are also present due to misalignment, and are conservatively estimated to be 25% of the motor force. Using Newton's law, the resulting acceleration is 78.6 m/s^2. This equates to a 193 millisecond engagement time, which is an acceptable result with a considerable safety factor. At a 5m fall height, assuming the body falls from rest, there is roughly 1 second of free fall. This shows acceptable results with a considerable safety factor.

6 RJC EVALUATION AND RESULTS

6.1 Yield Strength

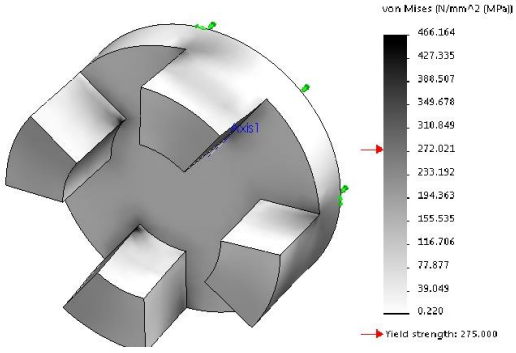

Figure 10: Solidworks FEA analysis of RJC

The maximum yield strength of the RJC was evaluated using the Solidworks static analysis tool. Figure 11 shows the finite element results using a jaw with the minimum required dimensions and

an applied external torque of 800 Nm. The yield strength was not reached in the simulation.

6.2 Engagement Time

A prototype of the RJC to test engagement time was fabricated in 3D-printed ABS. A 16 mm extension spring with a spring constant of 0.23 N/mm was used to connect the spider and the jaw. A 6V 50:1 Pololu micro metal gearmotor with a 12 CPR magnetic encoder was used to actuate the jaw, powered by a L298 Dual H-Bridge motor driver. An Arduino Uno microprocessor was used to sample the encoder data. Using this 3D printed setup, we found the engagement time of our device to be 146 milliseconds at 6V, validating that the design provides sufficient engagement speeds.

7 FUTURE WORK

7.1 Integration

The two proposed mechanisms in this paper have been designed to greatly increase the capabilities of the planetary exploration robot SUPERball. The BDSLC prototype was shown to be able to withstand up to at least 12 Nm. Additionally, simulation of the RJC shows that it can withstand up to 400 Nm of torque, which exceeds the amount of torque needed to protect the drivetrain from cable tensions during deployment. With a demonstrated engagement time of less than 150 ms, the modified Scotch yolk makes the RJC fast enough to respond to unexpected falls that would overwhelm the BDSLC.

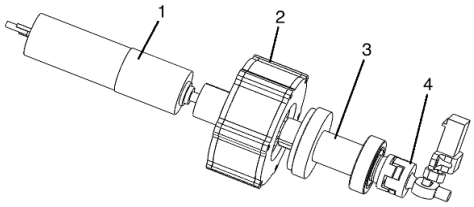

Figure 11: An integration scheme with the BDSLC and RJC in series

The next step in the design process is creating an integrated system in which both mechanisms work in series. Figure 11 outlines a possible integration scheme. The motor (1) connects directly to the input of the BDSLC (2). The output of the BDSLC is connected to the cable spool (3) via a series elastic element, such as a torsion spring, and the spool is constrained with a rotational ball bearing (4). The jaw of the RJC (4) is designed directly into end the spool. In this setup, a torsionally elastic element between the spool and the BDSLC would be needed to ensure cable forces fully dissipate into the RJC when it is engaged.

7.2 Scalability

Future iterations of SUPERball may have larger masses to which both mechanisms presented in this paper are easily scalable. The RJC could be scaled to withstand higher torques by increasing the outer diameter or tooth thickness. Switching to a stronger material, would also increase the torque rating. There are a number of ways that the BDSLC can be scaled to higher torque ratings. Increasing the number of wedged rollers would increase its strength, because the output torque is evenly distributed. A BDSLC with a larger diameter decreases force on each roller, would allow room for more rollers, and would allow for larger RG. Additionally, using a harder material for the output cam and the outer race would increase the torque rating.

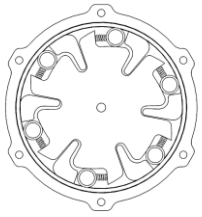

Figure 12: One directional self-locking clutch

The BDSLC could be replaced with a one-directional system, such as the one presented in Figure 12. As cables only transmit force in tension, braking can be prevented in one direction. Thus the torque capabilities could be increased with the same basic inner relationships. A one-directional self-locking clutch is being designed and tested at NASA Ames currently.

Appendix

The following are estimations for the specifications of SUPERball's next prototype: 40kg total mass m, 9450 K/m spring constant K, gravity of 9.81 g and 9mm spool radius r. Two assumptions are made, all of SUPERball's kinetic energy is transferred instantly into a single cable and drag and horizontal motion are negligible.

Two heights H, 50 m and 5 m, were selected to be appropriate drop test heights for SUPERball's capabilities. These heights can be used in the potential energy equation, thus finding the total energy. Applying this in A2, the torque on the spool is found. The high and low heights yield a torque of 160 and 50 Nm. Cable tension equal the torque divided by the spool radius. Falling time can be found using A3. The time for a 5m drop is 1.01 seconds.

$$T = r * k * \sqrt{\frac{2E}{K}}$$

$$t = \sqrt{\frac{2H}{g}}$$

However, the torque ratings of 160 Nm and 50 Nm were not used in the design of these components. The BDSLC will eventually be replaced with a unidirectional system. Therefore the current iteration only needs to handle 25 Nm. It will be replaced by a device of the same size and inertia but roughly double the torque capacity. The RJC was designed to handle 400 Nm instead of the minimum 160 Nm. A rough estimate of possible terminal velocity suggested that a 400 Nm torque rating might indeed prove to suffice for possible off planet missions, as the increase in size was minimal, the 400 Nm rating was used throughout.

Acknowledgement

We would like to acknowledge the NASA Ames SpaceShop, and in particular Alex Mazhari, for their help with the development. We appreciate the Titan Black GPU donation from NVIDIA Corporation. Thank you to the Dynamic Tensegrity Lab members for their help with design and testing, and for IRG's support to our research on tensegrity mechanisms.

References

[1] Plooij, M., Mathijssen, G., Cherelle, P., Lefeber, D., \& Vanderborght, B. (2015). Lock Your Robot: Review of Locking Devices in Robotics. Robotics \& Automation Magazine, IEEE, 22(1), 106-117.

[2] Joshi, B., \&. Al-Hakkak, F. (2015). An Introduction to Tensegrity Structures.

[3] Sabelhaus, A. P., Bruce, J., Caluwaerts, K., Manovi, P., Firoozi, R. F., Dobi, S., Agogino, A., \& SunSpiral, V. (2015, May). System design and locomotion of SUPERball, an untethered tensegrity robot. In Robotics and Automation, 2015 IEEE International Conference on (pp. 2867-2873). IEEE.

[4] Bruce, J., Sabelhaus, A., Chen, Y., Lu, D., Morse, K., Milam, S., ... \& SunSpiral, V. (2014). Superball: Exploring tensegrities for planetary probes. In 12th International Symposium on Artificial Intelligence, Robotics and Automation in Space (i-SAIRAS).

[5] J. Friesen, P. Glick, M. Fanton, P. Manovi, A. Xydes, T. Bewley \& V. Sunspiral, "The Second Generation Prototype of a Duct Climbing Tensegrity", under review in IEEE International Confrence on Robotics and Automation (ICRA), 2016

[6] Controzzi, M., Cipriani, C., \& Carrozza, M. C. (2010). Miniaturized non-back-drivable mechanism for robotic applications. Mechanism and Machine Theory,45(10), 1395-1406.

[7] Kapelevich, A. L., \& Taye, R. (2010). Self--Locking Gears: Design and Potential Applications.

[8] In, H., Kang, S., \& Cho, K. J. (2012, October). Capstan brake: Passive brake for tendon-driven mechanism. In Intelligent Robots and Systems (IROS), 2012 IEEE/RSJ International Conference on (pp. 2301-2306). IEEE.

[9] Montagnani, F., Controzzi, M., \& Cipriani, C. (2015). Non-back-drivable rotary mechanism with intrinsic compliance for robotic thumb abduction/adduction. Advanced Robotics, 29(8), 561-571.

[10] Orthwein, W. C. (2004). Clutches and brakes: design and selection. CRC Press.

[11] Chu, J. U., Jung, D. H., \& Lee, Y. J. (2008, May). Design and control of a multifunction myoelectric hand with new adaptive grasping and self-locking mechanisms. In Robotics and Automation, 2008. ICRA 2008. IEEE International Conference on (pp. 743-748). IEEE.

[12] Sirisopha, W., \& Suthakorn, J. A Study of Rotary-Brake Design for Utilizing in Motorized Upper Limb Prosthesis.

[13] Johnson, K. L., \& Johnson, K. L. (1987). Contact mechanics. Cambridge university press.

[14] G. van Oort, R. Carloni, D. J. Borgerink, and S. Stramigioli, "An energy efficient knee locking mechanism for a dynamically walking robot," in Proc. IEEE Int. Conf. Robotics Automation, 2011, pp. 2003–2008.

[15] S. Collins and A. Ruina, "A bipedal walking robot with efficient and human-like gait," in Robotics and Automation, 2005. ICRA 2005. Proceedings of the 2005 IEEE International Conference on, April 2005, pp. 1983– 1988.

[16] Tavakoli, M., Marques, L., \& De Almeida, A. T. (2013, November). Flexirigid, a novel two phase flexible gripper. In Intelligent Robots and Systems (IROS), 2013 IEEE/RSJ International Conference on (pp. 5046-5051). IEEE.

[17] B. Li, Q. Deng, and Z. Liu, "A spherical hopping robot for exploration in complex environments," in IEEE International Conference on Robotics and Biomimetics, 2009, pp. 402–407.

[18] B. Brackx, M. Van Damme, A. Matthys, B. Vander- borght, and D. Lefeber, "Passive ankle-foot prosthesis prototype with extended push-off," Int J Adv Robotic Sy, vol. 10, no. 101, 2013.

[19] A. Kossett and N. Papanikolopoulos, "A robust miniature robot design for land/air hybrid locomotion," in IEEE International Conference on Robotics and Automation, 2011, pp. 4595–4600.

[20] J. Hao, "Material Handbook, Material Properties and Applications" 2010

[21] O.A. Leutwiler, "Elements of Machine Design" 1917